Research Article Vol. 32, No. 12 / 3 Jun 2024 / Optics Express 21497
Optics EXPRESS

Suppressing the radiation loss by hybrid Tamm-surface plasmon BIC modes

TONG QIAO,[1] MENGYING HU,[2] QIANG WANG,[1] MENG XIAO,[3,4] SHINING ZHU,[1] AND HUI LIU[1,*]

[1]National Laboratory of Solid State Microstructures, School of Physics, Collaborative Innovation Center of Advanced Microstructures, Nanjing University, 210093 Nanjing, China
[2]Department of Physics, State Key Laboratory of Surface Physics, and Key Laboratory of Micro and Nano Photonic Structures (Ministry of Education), Fudan University, Shanghai 200438, China
[3]Key Laboratory of Artificial Micro- and Nano-structures of Ministry of Education and School of Physics and Technology, Wuhan University, 430072 Wuhan, China
[4]Wuhan Institute of Quantum Technology, Wuhan 430206, China
*huiliu@nju.edu.cn

Abstract: Tamm plasmon polaritons (TPPs), localized near the boundary of a dielectric Bragg reflector (DBR) and a thin metal film, have attracted much attention for the lower ohm loss and flexible excitation. However, the radiation loss resulting from the direct coupling to the surroundings hinders their applications. Here, we propose and experimentally demonstrate a new type of hybrid plasmonic quasi-bound state in the continuum (BIC) in a Tamm-surface plasmon polariton system to suppress the radiation loss. Leveraging the scattering of the periodic metal array, the TPP interacts with the surface plasmon polariton (SPP) mode and form a Friedrich-Wintgen type quasi-BIC state that originated from the interference of two surface waves with different natures. Through angle resolved reflectance spectrum measurement, the hybrid plasmonic quasi-BIC was observed in the experiment. Our work proposes a new method to design a high Q mode in plasmonic systems, and thus holds promise for applications in the field of light matter interactions.

© 2024 Optica Publishing Group under the terms of the Optica Open Access Publishing Agreement

1. Introduction

In recent decades, surface plasmon polaritons (SPPs) have emerged as a captivating research area in optics [1,2]. Benefitting of strong optical field localization and enhancement, SPPs find widespread applications in the realms of integrated optics, nonlinear optics, and optical imaging or trapping [3–5]. Nevertheless, the ohmic loss induced by the metallic structures in SPPs cause the inevitable energy dissipations [6,7], limiting their on its practical application range. Recently, Tamm plasmon polaritons (TPPs), localized at the boundary of a dielectric photonic crystals(PCs) and a thin metal film, has been proposed by researchers [8]. Compared with conventional SPPs, TPPs inherit the advantages of field enhancement and have both TE/TM modes simultaneously, which can be excited by free space light directly without the need for diffraction gratings or prisms, as required in SPPs cases. These properties are exploited for perfect absorption, TPP lasers, enhancement of spontaneous emission, nonlinear and topological effects [9–27], etc. However, these TPP based devices are susceptible to considerable radiation loss owing to the direct coupling with the light in the surrounding [24–27], which hinder their further applications.

On the other hand, bound states in the continuum (BICs) have drawn great attention due to divergent Q factor [28–30]. According to their mechanism, BICs can be classified into different categories and exploited in various physical systems, such as parameters finetuning BICs, symmetry-protected BICs, and inversed constructed BICs [31]. So far, there are numerous implementations of BICs in dielectric systems, including photonic crystals/slabs, resonators and waveguide arrays [30,32–55], etc. In addition, researchers have also extended the concept of

#525338 https://doi.org/10.1364/OE.525338
Journal © 2024 Received 3 Apr 2024; revised 19 May 2024; accepted 19 May 2024; published 28 May 2024

Optics EXPRESS

BICs to quasi-BICs by introducing perturbations or in lossy system to obtained high-Q modes [33,39–40]. For example, Azzam et al. proposed a hybrid plasmon-photonic system to realize Friedrich-Wintgen type quasi-BICs (FW-BICs) with metallic structures [49,50]. Then related experimental implementations have been realized and beneficiated the attainability of lower-loss modes [51,52], and high Q TPP or hybrid TPP mode interacting with BIC were demonstrated the potential application in optical lasing, optical sensing and quantum photonic devices [53–58]. However, the exploration of BICs in lossy systems are limited in the plasmon-photonic system, and there is no report on the hybrid plasmonic system, especially for the TPPs and SPPs, which may open a route to suppress the radiation loss and provide new engineering methods for the low-loss TPPs with flexible tunability.

In this work we proposed a new mechanism to suppress the radiation loss and realize high Q Tamm states by engineering the BIC in a coupled TPPs-SPPs system. The system was composed of photonic crystals and a metal film with periodic etched holes. Through meticulous design, we acquire tunable couplings between TPP and SPP, which mainly locates at the boundary of PCs and metal structures. The TPP residing in the photonic bandgap will have overlap with the SPP that folded by the periodical arrays. Hence, an anti-crossing plasmonic bandgap forms with the hybrid modes depressing the radiation loss. By changing the lattice period, the coupling strength can be tuned for the plasmonic bandgaps. Particularly, a hybrid plasmonic mode with the radiation loss can be reduced to near zero while another hybrid mode is lossy. Thus we realize a FW-BIC state associated with the anti-crossing bandgap [58]. These results have been demonstrated in the angle-resolved reflection experiment and agree well with the simulated results from an theoretical coupled model. The experimental quality factor will reach nearly 280, indicating a high density of optical states. Our design holds great potential applications in photonic laser beams, strong coupling region between quantum emitters and photonic cavities in nonlinear optics [59,60].

2. Results and discussion

Fig. 1(a) shows the schematic of a plasmonic lattice composed of a PC and two-dimensional periodical metallic arrays. As shown in Fig. 1(a), the designed PC structure comprises 12 unit cells, each consisting of three layers labeled as A/2-B-A/2. Here, layer A is HfO_2 and layer B is SiO_2. The thickness of HfO_2 is 133 nm and the SiO_2 layer is 182 nm with refractive indices of 2 and 1.46, respectively [61]. Instead of utilizing a thin metallic film as in usual Tamm devices, we patterned two dimensional periodical metallic arrays on top of the PC, shown as the yellow part. The square hole array is etched from a silver film with a period L and the diameter d, as displayed in Fig. 1(b). The etching depth goes into the first layer dielectric materials, which is necessary to realize a stronger coupling between TPP and SPP modes reducing the energy loss of the Tamm confined mode in the visible and infrared regime [19,24].

In the experiment, the PC is grown by electron beam evaporation deposition on a silicon dioxide substrate. After depositing a 30nm-thick Si_3N_4 film on top of the PC, gratings are etched from a 50nm-thick silver film on the Si_3N_4 film using a focused ion beam (FIB, 30 keV 40 pA). The etching depth is 100 nm. We fabricated the periodical structures with a period $L = 460$ nm and the hole diameter d is 230 nm. The scanning electron microscope (SEM) top view of the lattice sample is shown in Fig. 1(c). To experimentally demonstrate the band structures of the plasmon lattice, we introduce the angle-resolved micro spectroscopy system (ARMS) [62] to measure the reflection spectra of the sample, as illustrated in Fig. 1(d). The information of the radiation field of the sample in the Fourier space or momentum space is the same as that on the back focal plane of the objective lens. Due to the fact that the spectrometer is conjugated with the back focal plane of the objective lens, we are capable of obtaining the Fourier-transformed spectra. Then we can map the band structures of the sample in the entire First Brillouin zone

Optics EXPRESS

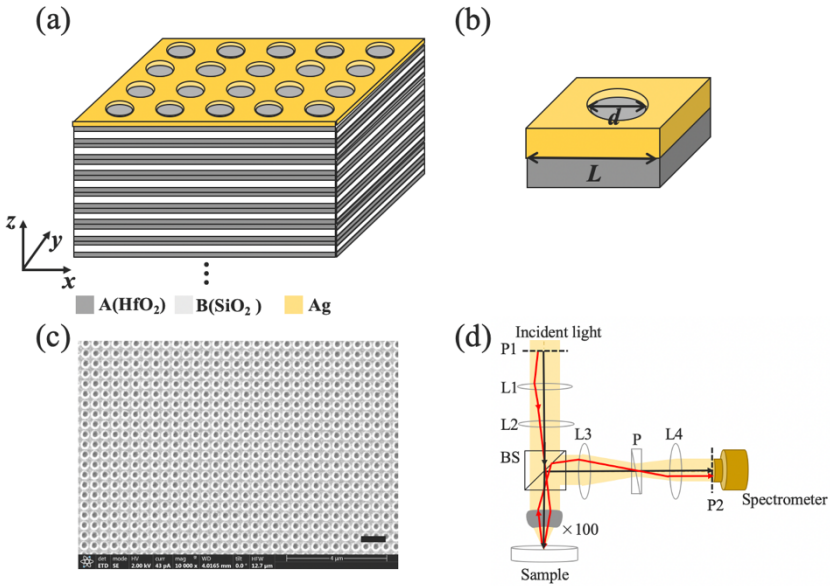

Fig. 1. Sample caption. (a) Schematic of the structure comprising multilayers and two dimensional periodical metallic arrays. Layers of HfO_2 (SiO_2) are depicted in gray (light gray) and labeled as 'A(B)'. The multilayers consist of 12 unit cells and each unit cell composes of three alternating layers: A/2, B and A/2. The yellow part deposited on top of the multilayer structure corresponds to the silver film with etching air holes. (b) Unit cell of the designed structure with the period L and the diameter d. Square array etching holes are inserted into the first layer dielectric materials with a height of 100 nm. (c) SEM top view of the fabricated sample. The scale bar inside the figure corresponds to a length of 1μm. (d) Setup of the experimental angle-resolved reflection spectrum system. Black arrow lines correspond to the normal incidence and reflectance while red lines are the oblique case. BS, beam splitter; L, lens; P, polarizer; P1, incident plane; P2, angle resolving plane.

within the visible regime by altering the injection position of the Xe lamp fiber source on the focal plane.

In order to get the dispersion of the lattice above, we use the commercial finite element simulation software (COMSOL Multiphysics) to calculate the y-polarized band structures of the lattice. The y polarized direction is parallel to the sample surface shown in Fig. 1(a). The calculated results are given as black circles in Fig. 2(a), in which the gray region refers to projected bulk bands of the PC. The white region corresponds to the bandgap of PC. The original Tamm dispersion marked by a light- yellow dashed line in Fig. 2(a) is a parabolic line inside the PC's bandgap. In general, the TPP dispersion in above the light line while SPP is under the light cone. However, due to the scattering of periodical structures, the Tamm band folds at the edge of the first Brillouin zone and forms a small Tamm bandgap as similar to a one-dimensional lattice [19]. Meanwhile, another band marked by a red dashed line starting from 330THz at $k_x = 0$ point is the folded SPP band coming from the region below the light cone. The SPP dispersion overlaps at $k_x = 0.445$ with the folding TPP mode represented and forms a coupled bandgap. The dispersion coupling process is shown in the enlarged Fig. 2(b), indicating the interaction between the TPP and SPP mode. This kind of bandgap mechanism that couples SPP and TPP, which original locate at two sides of light cone but fold into the PC's bandgap by the lattice, is different from the plasmon-photonic guide modes [49–52]. In addition, it should be noted that many dispersion splits can be found between 350-450THz in Figure 2(c), which corresponds to the coupled dispersion of folded TPP/SPP and bulk bands of PCs [19]. Detailed folded band

Optics EXPRESS

structures of the coupled process and field distribution of the two modes can be found in the Supplement 1.

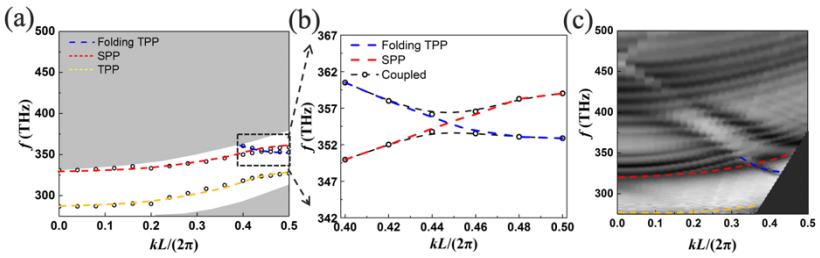

Fig. 2. (a) Simulated dispersion of TPP and SPP eigenmodes along the Γ-X direction for *y*-polarization shown in Fig. 1(a). The gray area indicates the region of projected bands of the multilayers. Black circles eyed by the yellow dashed line represent the TPP dispersion and the folding TPP modes are marked by a blue dashed line. SPP dispersion staring from 330THz inside the bandgap by the red dashed line couples with the folded TPP dispersion, resulting in a bandgap marked by the black dashed rectangular. (b) Enlarged calculated dispersion in the black dashed rectangular. Uncoupled SPP modes are exhibited by the red dashed line and the blue represents folded TPP, respectively. (c) Experimentally measured angle-resolved reflection spectrum for the sample in Fig. 1(c).

Experimentally, we measure angle-resolved reflection spectra harnessing the system sketched in Fig. 1(c) and the results of band structures under *y*-polarization are shown in Fig. 2(c). The TPP and SPP bands are labeled by blue and red lines for visual clarity, respectively. Two dispersions overlap inside the PC bandgap and a small coupled bandgap with a width of 4THz emerges, showing consistency with simulations. The TPP band with a lower frequency (near 275THz) is close to the spectra measurement limit, which is marked by the yellow dashed line in Fig. 2(c). The black area is marked by the boundary of the 60-degree light line limit determined by the maximum incident angle in ARMS measurement system.

Based on the plasmon lattice design above, we start to tune the plasmonic lattice to implement varying coupling effect. For the lattice structures in Fig. 2(a), we maintain the PC parameters and change the lattice period from 460 nm to 540 nm and 600 nm. During this process, the ratio of hole diameter to lattice period is fixed at 0.5. Here, the Tamm states field couples with propagated SPPs through the holes and the field overlap induces the coupling strength, which can be tuned by the hole size(see details in the Supplement 1). Meanwhile, proper period design will provide help with the folding dispersion interaction inside the middle location of photonics bandgap, avoiding the unexpected leaking phenomena in the PC's bulk bands. In experiments, we utilize the angle-resolved reflection spectrum system to investigate the dispersion of the plasmon lattice. The sample is fabricated using a similar approach as we employ in Fig. 2. The etching depth is consistent for all the samples. In Fig. 3(a)-(c), we plot the experimentally measured angle-resolved reflection spectra for different period lattices under the *y*-polarized excitation. The periods of unit cells are 460 nm, 540 nm and 600 nm in Fig. 3(a)-(c), respectively. The formed coupled bandgap is well preserved, indicating the continuous consistency of the manufacturing quality of our samples. The TPP-SPP coupled plasmonic bandgap is broadening with an increasing lattice period, which indicates the stronger coupling strength.

In order to gain a deeper insight into the physical process, we introduced a coupled model with two energy levels, incorporating loss terms in the Hamiltonian to describe the system:

$$H(k_x) = \begin{pmatrix} E_+(k_x) & U \\ U & E_-(k_x) \end{pmatrix} - i\begin{pmatrix} \Gamma_1 & \Gamma \\ \Gamma & \Gamma_2 \end{pmatrix} \tag{1}$$

Optics EXPRESS

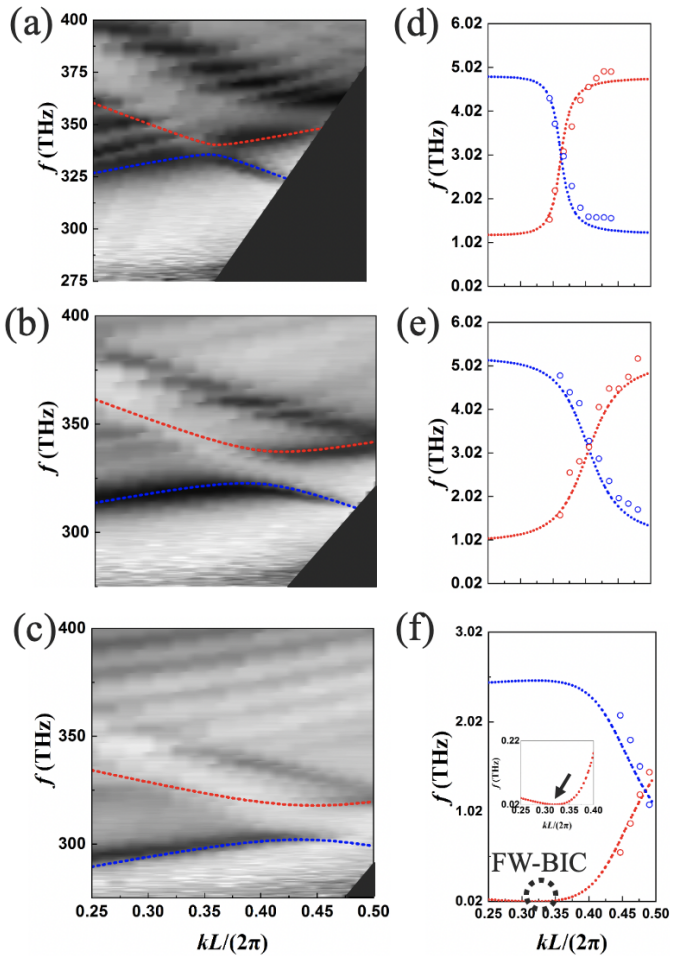

Fig. 3. (a)-(c) Experimentally measured angle-resolved reflection spectra including the calculated results under *y*-polarized excitation. The periods of unit cells are: (a) $L = 460$ nm; (b) $L = 540$ nm; (c) $L = 600$ nm. Simulated dispersions (the red and blue dashed lines) are overlaid on the experimental angle-resolved data. The range of incident angle is from 0 to 60 degree. (d)-(f) Calculated (dashed lines) imaginary part of dispersions using the coupled model and the corresponding data fitted from the experimental results (circle dots). The black circle marks the FW-BIC point. The inset figure in (f) is the enlarged dispersion near the BIC point.

Here E_+ and E_- represent the energy of the TPP and SPP modes, respectively. Γ_1 and Γ_2 denote the losses of the Tamm and surface plasmonic modes. U is the coupling strength and Γ is the anti-crossing coupling term in the imaginary part, which can be controlled by the loss variation in two radiation loss channels to far field. Thus, the dispersion of the two coupled modes, akin to that of a lossy two-levels system, can be obtained from the diagonalized Hamiltonian in the Equation (1):

$$H_+ = \frac{\omega_1 + \omega_2}{2} - i\frac{\Gamma_1 + \Gamma_2}{2} + \sqrt{\left(\frac{(\omega_1 - \omega_2) - i(\Gamma_1 - \Gamma_2)}{2}\right)^2 + (U - i\Gamma)^2} \tag{2}$$

Optics EXPRESS

$$H_{-} = \frac{\omega_1 + \omega_2}{2} - i\frac{\Gamma_1 + \Gamma_2}{2} - \sqrt{\left(\frac{(\omega_1 - \omega_2) - i(\Gamma_1 - \Gamma_2)}{2}\right)^2 + (U - i\Gamma)^2} \quad (3)$$

Especially, when the condition $U(\Gamma_1 - \Gamma_2) = \Gamma(\omega_1 - \omega_2)$ is satisfied, the imaginary part of one hybrid mode will be minimum and the mode thus corresponds to an BIC point [31].

In Fig. 3(a)-(c), the red curve corresponds to the high-frequency mode, while the blue curve corresponds to the low-level mode. Three calculated dispersions with tuning coupling parameters are overlaid onto the experimental results and match well. In addition, we also present the imaginary dispersion obtained from the coupled model in Fig. 3(d)-(f). The normalized range of the wave vector is from 0.25 to 0.5 owing to the finite real lattice dispersion inside the PC's bandgap. Lines are obtained by the coupled model and circle dots are corresponding to the fitting with experiment results. The red and blue dispersions show opposite trend along the wave vector. Especially for the red mode, the lower imaginary part of eigenfrequency near the coupling central wavelength indicates lower loss and a better quality factor for the hybrid mode with higher frequency, observed in all three lattices. Furthermore, we notice that the red imaginary part of the eigenfrequency decreases with the increasing lattice period. Especially in Fig. 3(f), the imaginary dispersion will reach to a minimum point close to 0 at $kL/(2\mathrm{Pi}) = 0.33$, which means the FW condition is meet and corresponds to a FW-BIC point in such a system with material loss (see details in the Supplement 1). To further testify our argument above, we calculate the Q factor of the coupled lattice modes with higher frequency using the lossy coupled mode, which is represented by three dashed lines in the Fig. 4. The circles corresponding to the experimental data derived from the angle-resolved experiment with different lattice periods. The Q factor increases with a bigger lattice period and smaller wave vector, as predicted by the imaginary part simulation. The highest Q value can reach to 280. The simulated results agree well with the experiments.

It should be noted that TPP and SPP separated by a thin metallic film can form hybrid plasmonic modes and the coupling diminishes gradually with an increasing metal film thickness [55].The high-quality plasmonic mode here is achieved due to the coupling through the lattice, which provides a coupled channel between TPP and SPP. Limited by the inevitable material loss, the coupled system approaches to the bound state with high quality factors and the corresponding

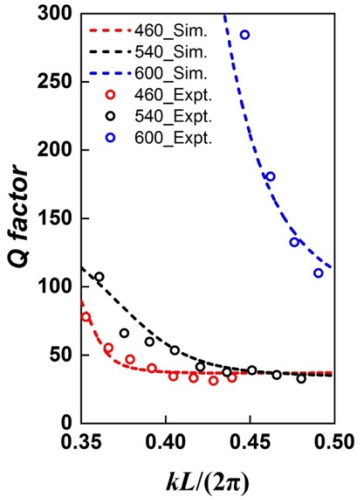

Fig. 4. Experimental Q factors of the hybrid plasmonic mode attained with different lattice periods $L = 460$ nm, 540 nm, and 600 nm, respectively. The dashed lines correspond to the simulated results using the coupled model.

Optics EXPRESS

imaginary part of eigen-frequency is very small, which is different from the pure dielectric system. Compared to the SPP system, the coupled lattice inherits the lower loss in TPP and simultaneously suppresses the radiation loss to the far field through the coupled lattice. More intriguingly, it can be flexibly manipulated by tuning the geometric parameters such as the etching depth or period so as to control the coupling between two confined fields. This proposed system provides an effective way to design tunable and low-loss plasmonic devices and suggests the applications in plasmonic systems with high-quality modes, such as sensing detection, lasing and nonlinear effects.

3. Conclusion

In summary, we report a hybrid coupled plasmon lattice in this work, which is formed by photonic crystals and metallic arrays. Through the coupling between TPPs and SPPs, a plasmonic bandgap is generated. By changing the period of the lattice, the coupling between can be tuned to realize a FW-BIC described by a coupled model. In this process, the bandwidth of one hybrid mode can be reduced by suppressing the radiation loss and lead to high quality factors. All the results can be directly measured using the angular resolved reflection spectrum. This system can be used to manipulate the light-matter interaction, and has promising applications in the fields of nonlinear optics and quantum optics.

Funding. National Natural Science Foundation of China (12334015, 62288101, 92150302, 92163216); National Key Research and Development Program of China (2017YFA0205700, 2017YFA0303702); Outstanding Ph.D. Candidate of Nanjing University (Program B).

Acknowledgments. The authors acknowledge Micro/nano Optical Characterization and Measurement Center of NJU for the experimental measurements.

Disclosures. The authors declare no conflicts of interest.

Data availability. Data underlying the results presented in this paper are not publicly available at this time but may be obtained from the authors upon reasonable request.

Supplemental document. See Supplement 1 for supporting content.

References

1. S. A. Maier, *Plasmonics: Fundamentals and Applications* (Springer, 2007), Vol. 1.
2. J. A. Schuller, E. S. Barnard, W. Cai, *et al.*, "Plasmonics for extreme light concentration and manipulation," Nat. Mater. **9**(3), 193–204 (2010).
3. M. Kauranen and A. V. Zayats, "Nonlinear plasmonics," Nat. Photonics **6**(11), 737–748 (2012).
4. Y. Zhang, J. Shen, C. Min, *et al.*, "Nonlinearity-induced multiplexed optical trapping and manipulation with femtosecond vector beams," Nano Lett. **18**(9), 5538–5543 (2018).
5. Y. Zhang, C. Min, X. Dou, *et al.*, "Plasmonic tweezers: for nanoscale optical trapping and beyond," Light: Sci. Appl. **10**(1), 59 (2021).
6. A. Boltasseva and H. A. Atwater, "Low-loss plasmonic metamaterials," Science **331**(6015), 290–291 (2011).
7. J. B. Khurgin, "How to deal with the loss in plasmonics and metamaterials," Nat. Nanotechnol. **10**(1), 2–6 (2015).
8. M. Kaliteevski, I. Iorsh, S. Brand, *et al.*, "Tamm plasmon-polaritons: Possible electromagnetic states at the interface of a metal and a dielectric Bragg mirror," Phys. Rev. B **76**(16), 165415 (2007).
9. M. Sasin, R. Seisyan, M. Kalitteevski, *et al.*, "Tamm plasmon polaritons: Slow and spatially compact light," Appl. Phys. Lett. **92**(25), 251112 (2008).
10. Y. Gong, X. Liu, H. Lu, *et al.*, "Perfect absorber supported by optical Tamm states in plasmonic waveguide," Opt. Express **19**(19), 18393–18398 (2011).
11. O. Gazzano, S. M. de Vasconcellos, K. Gauthron, *et al.*, "Evidence for Confined Tamm Plasmon Modes under Metallic Microdisks and Application to the Control of Spontaneous Optical Emission," Phys. Rev. Lett. **107**(24), 247402 (2011).
12. C. Symonds, G. Lheureux, J. Hugonin, *et al.*, "Confined Tamm Plasmon Lasers," Nano Lett. **13**(7), 3179–3184 (2013).
13. G. Lheureux, S. Azzini, C. Symonds, *et al.*, "Polarization-controlled confined Tamm plasmon lasers," ACS Photonics **2**(7), 842–848 (2015).
14. Q. Wang, M. Xiao, H. Liu, *et al.*, "Measurement of the Zak phase of photonic bands through the interface states of a metasurface/photonic crystal," Phys. Rev. B **93**(4), 041415 (2016).
15. Y. Tsurimaki, J. K. Tong, V. N. Boriskin, *et al.*, "Topological Engineering of Interfacial Optical Tamm States for Highly Sensitive Near-Singular-Phase Optical Detection," ACS Photonics **5**(3), 929–938 (2018).

Optics EXPRESS

16. H. Lu, Y. Li, H. Jiao, *et al.*, "Induced reflection in Tamm plasmon systems," Opt. Express **27**(4), 5383–5392 (2019).
17. E. Buzavaite-Verteliene, A. Valavicius, L. Grineviciute, *et al.*, "Influence of the graphene layer on the strong coupling in the hybrid Tamm-plasmon polariton mode," Opt. Express **28**(7), 10308–10319 (2020).
18. E. Buzavaite-Verteliene, I. Plikusiene, T. Tolenis, *et al.*, "Hybrid Tamm-surface plasmon polariton mode for highly sensitive detection of protein interactions," Opt. Express **28**(20), 29033–29043 (2020).
19. T. Qiao, M. Hu, X. Jiang, *et al.*, "Generation and tunability of supermodes in tamm plasmon topological superlattices," ACS Photonics **8**(7), 2095–2102 (2021).
20. J. Han, Y. Shao, C. Chen, *et al.*, "Tunable dual-band mid-infrared absorber based on the coupling of a graphene surface plasmon polariton and Tamm phonon-polariton," Opt. Express **29**(10), 15228–15238 (2021).
21. S. Zumrat, S. Shahid, and M. A. Talukder, "Dual-wavelength hybrid Tamm plasmonic laser," Opt. Express **30**(14), 25234–25248 (2022).
22. Z. Hu, T. Krisnanda, A. Fieramosca, *et al.*, "Energy transfer driven brightening of MoS2 by ultrafast polariton relaxation in microcavity MoS2/hBN/WS2 heterostructures," Nat. Commun. **15**(1), 1747 (2024).
23. Y. García-Puente, B. Auguié, and R. Kashyap, "High-Q Tamm plasmon-like resonance in spherical Bragg microcavity resonators," Opt. Express **32**(6), 9644–9655 (2024).
24. L. Ferrier, H. S. Nguyen, C. Jamois, *et al.*, "Tamm plasmon photonic crystals: From bandgap engineering to defect cavity," APL Photonics **4**(10), 106101 (2019).
25. V. Toanen, C. Symonds, J. M. Benoit, *et al.*, "Room-Temperature Lasing in a Low-Loss Tamm Plasmon Cavity," ACS Photonics **7**(11), 2952–2957 (2020).
26. O. Buchnev, A. Belosludtsev, V. Reshetnyak, *et al.*, "Observing and controlling a Tamm plasmon at the interface with a metasurface," Nanophotonics **9**(4), 897–903 (2020).
27. R. G. Bikbaev, D. N. Maksimov, P. S. Pankin, *et al.*, "Critical coupling vortex with grating-induced high Q-factor optical Tamm states," Opt. Express **29**(3), 4672–4680 (2021).
28. S. Zhang, Z. Ye, Y. Wang, *et al.*, "Anti-Hermitian plasmon coupling of an array of gold thin-film antennas for controlling light at the nanoscale," Phys. Rev. Lett. **109**(19), 193902 (2012).
29. B. Zhen, C. W. Hsu, L. Lu, *et al.*, "Topological nature of optical bound states in the continuum," Phys. Rev. Lett. **113**(25), 257401 (2014).
30. C. W. Hsu, B. Zhen, J. Lee, *et al.*, "Observation of trapped light within the radiation continuum," Nature **499**(7457), 188–191 (2013).
31. C. W. Hsu, B. Zhen, A. D. Stone, *et al.*, "Bound states in the continuum," Nat. Rev. Mater. **1**(9), 16048–13 (2016).
32. Y. X. Xiao, G. Ma, Z. Zhang, *et al.*, "Topological subspace-induced bound state in the continuum," Phys. Rev. Lett. **118**(16), 166803 (2017).
33. K. Koshelev, S. Lepeshov, M. Liu, *et al.*, "Asymmetric metasurfaces with high-Q resonances governed by bound states in the continuum," Phys. Rev. Lett. **121**(19), 193903 (2018).
34. H. M. Doeleman, F. Monticone, W. den Hollander, *et al.*, "Experimental observation of a polarization vortex at an optical bound state in the continuum," Nat. Photonics **12**(7), 397–401 (2018).
35. W. Liu, B. Wang, Y. Zhang, *et al.*, "Circularly polarized states spawning from bound states in the continuum," Phys. Rev. Lett. **123**(11), 116104 (2019).
36. B. Wang, W. Liu, M. Zhao, *et al.*, "Generating optical vortex beams by momentum-space polarization vortices centred at bound states in the continuum," Nat. Photonics **14**(10), 623–628 (2020).
37. X. Yin, J. Jin, M. Soljačić, *et al.*, "Observation of topologically enabled unidirectional guided resonances," Nature **580**(7804), 467–471 (2020).
38. M. V. Gorkunov, A. Alexander, Yuri S. Kivshar, *et al.*, "Metasurfaces with maximum chirality empowered by bound states in the continuum," Phys. Rev. Lett. **125**(9), 093903 (2020).
39. N. Bernhardt, K. Koshelev, S. J. White, *et al.*, "Quasi-BIC resonant enhancement of second-harmonic generation in WS2 monolayers," Nano Lett. **20**(7), 5309–5314 (2020).
40. E. Melik-Gaykazyan, K. Koshelev, J. H. Choi, *et al.*, "From Fano to quasi-BIC resonances in individual dielectric nanoantennas," Nano Lett. **21**(4), 1765–1771 (2021).
41. A. Cerjan, M. Jürgensen, W. A. Benalcazar, *et al.*, "Observation of a higher-order topological bound state in the continuum," Phys. Rev. Lett. **125**(21), 213901 (2020).
42. A. Cerjan, C. Jörg, S. Vaidya, *et al.*, "Observation of bound states in the continuum embedded in symmetry bandgaps," Sci. Adv. **7**(52), eabk1117 (2021).
43. Y. Zeng, G. Hu, K. Liu, *et al.*, "Dynamics of topological polarization singularity in momentum space," Phys. Rev. Lett. **127**(17), 176101 (2021).
44. X. Xiao, Y. Lu, J. Jiang, *et al.*, "Manipulation of optical bound states in the continuum in a metal-dielectric hybrid nanostructure," Photonics Res. **10**(11), 2526–2531 (2022).
45. H. Chen, H. Wang, K. Wong, *et al.*, "High-Q localized surface plasmon resonance based on bound states in the continuum for enhanced refractive index sensing," Opt. Lett. **47**(3), 609–612 (2022).
46. F. Cao, M. Zhou, C. Cheng, *et al.*, "Interaction of plasmonic bound states in the continuum," Photonics Res. **11**(5), 724–731 (2023).
47. H. Ma, J. Niu, B. Gao, *et al.*, "Tunable metasurface based on plasmonic quasi bound state in the continuum driven by metallic quantum wells," Adv. Opt. Mater. **11**(5), 2202584 (2023).

Optics EXPRESS

48. Y. Chen, H. Deng, X. Sha, *et al.*, "Observation of intrinsic chiral bound states in the continuum," Nature **613**(7944), 474–478 (2023).
49. X. Gao, C. W. Hsu, B. Zhen, *et al.*, "Formation mechanism of guided resonances and bound states in the continuum in photonic crystal slabs," Sci. Rep. **6**(1), 31908 (2016).
50. S. I. Azzam, V. M. Shalaev, A. Boltasseva, *et al.*, "Formation of bound states in the continuum in hybrid plasmonic-photonic systems," Phys. Rev. Lett. **121**(25), 253901 (2018).
51. M. Meudt, C. Bogiadzi, K. Wrobel, *et al.*, "Hybrid photonic–plasmonic bound states in continuum for enhanced light manipulation," Adv. Opt. Mater. **8**(20), 2000898 (2020).
52. S. Joseph, S. Sarkar, S. Khan, *et al.*, "Exploring the optical bound state in the continuum in a dielectric grating coupled plasmonic hybrid system," Adv. Opt. Mater. **9**(8), 2001895 (2021).
53. D. S. Buzin, P. S. Pankin, D. N. Maksimov, *et al.*, "Hybrid Tamm and quasi-BIC microcavity modes," Nanoscale **15**(41), 16706–16714 (2023).
54. G. A. Romanenko, P. S. Pankin, D. S. Buzin, *et al.*, "Metal–dielectric optical microcavity with tunable Q factor," Appl. Phys. Lett. **123**(6), 061113 (2023).
55. B. I. Afinogenov, V. O. Bessonov, A. A. Nikulin, *et al.*, "Observation of hybrid state of Tamm and surface plasmon-polaritons in one-dimensional photonic crystals," Appl. Phys. Lett. **103**(6), 061112 (2013).
56. T. C. Tan, Y. K. Srivastava, R. T. Ako, *et al.*, "Active control of nanodielectric-induced THz quasi-BIC in flexible metasurfaces: a platform for modulation and sensing," Adv. Mater. **33**(27), 2100836 (2021).
57. M. Kang, T. Liu, C. T. Chan, *et al.*, "Applications of bound states in the continuum in photonics," Nat. Rev. Phys. **5**(11), 659–678 (2023).
58. C. Schiattarella, S. Romano, I. Sirleto, *et al.*, "Directive giant up conversion by supercritical bound states in the continuum," Nature **626**(8000), 765–771 (2024).
59. M. Hensen, T. Heilpern, S. K. Gray, *et al.*, "Strong coupling and entanglement of quantum emitters embedded in a nanoantenna-enhanced plasmonic cavity," ACS Photonics **5**(1), 240–248 (2018).
60. G. Arregui, J. Gomis-Bresco, T. Sotomayor, *et al.*, "Quantifying the Robustness of Topological Slow Light," Phys. Rev. Lett. **126**(2), 027403 (2021).
61. E. D. Palik, *Handbook of Optical Constants of Solids* (Academic Press, 1998), Vol. 3.
62. Y. Zhang, A. Chen, W. Liu, *et al.*, "Observation of Polarization Vortices in Momentum Space.," Phys. Rev. Lett. **120**(18), 186103 (2018).

117.111.2.206 {ts '2024-05-28 21:56:39'}